第 44 卷第 6 期　　硅　酸　盐　学　报　　Vol. 44，No. 6
2016 年 6 月　　JOURNAL OF THE CHINESE CERAMIC SOCIETY　　June，2016
http://www.gxyb.cbpt.cnki.net　　**DOI**：10.14062/j.issn.0454-5648.2016.06.15

# 氧化石墨烯–镝掺杂二氧化钛复合光催化材料制备及光催化性能

李翠霞，吴强红，曾鹏飞，谭高伟

(兰州理工大学，省部共建有色金属先进加工与再利用国家重点实验室，材料工程国家级实验教学示范中心，兰州 730050)

**摘　要**：以氧化石墨烯(GO)、钛酸四丁酯和硝酸镝为原料，用柠檬酸络合溶胶–凝胶法原位合成氧化石墨烯–镝掺杂二氧化钛($GO/D_y^{3+}–TiO_2$)，再经硼氢化钠还原得到还原氧化石墨烯–镝掺杂二氧化钛($rGO/D_y^{3+}–TiO_2$)复合光催化剂。利用 X 射线衍射、透射电子显微镜、Raman 光谱、荧光光谱对 $rGO/D_y^{3+}–TiO_2$ 样品进行分析表征。研究了 GO 的引入对 $TiO_2$ 晶体结构、形貌、光生载流子寿命和光催化活性的影响。结果表明：锐钛矿相 $D_y^{3+}–TiO_2$ 呈纳米颗粒状均匀分布在 *r*GO 表面；GO 的引入可抑制 $TiO_2$ 晶粒长大及从锐钛矿向金红石的相变；$rGO/D_y^{3+}–TiO_2$ 复合光催化剂的光催化活性明显高于 $D_y^{3+}–TiO_2$。

**关键词**：二氧化钛；镝掺杂；还原氧化石墨烯；柠檬酸；光催化
**中图分类号**：TB34　　**文献标志码**：A　　**文章编号**：0454–5648(2016)06–0874–06
**网络出版时间**：　　**网络出版地址**：

## Preparation and Photocatalytic Properties of $rGO/D_y^{3+}–TiO_2$ Composites

*LI Cuixia*, *WU Qianghong*, *ZENG Pengfei*, *TAN Gaowei*
(Lanzhou University of Technology, Key Laboratory of Advanced Processing and Recycling of Non-ferrous Metals, National Experimental Teaching Demonstration Center of Material Engineering, Lanzhou 730050, China)

**Abstract:** Dysprosium-doped titanium dioxide-decorated graphene oxide ($GO/D_y^{3+}–TiO_2$) was prepared with graphene oxide (GO), tetrabutyl titanate and dysprosium nitrate as precursors using an *in-situ* method of synthesis *via* a citric acid chelating sol–gel step. Afterwards, dysprosium doped titanium dioxide and reduced graphene oxide ($rGO/D_y^{3+}–TiO_2$) composite photocatalysts were obtained *via* a sodium borohydride reduction method. The composite materials were characterized by X-ray diffraction, transmission electron microscopy, Raman spectroscopy and photoluminescence spectroscopy, respectively. The effect of GO on the crystal structure of $TiO_2$, the lifetime of photogenerated carriers, and the morphology and photocatalytic activity of composite photocatalysts was investigated. The results show that $D_y^{3+}–TiO_2$ nanoparticles with anatase phase are well dispersed on the surface of the *r*GO sheets. The introduction of GO inhibits the grain growth of $TiO_2$ and the phase transformation from anatase to rutile. The photocatalytic activity of $rGO/D_y^{3+}–TiO_2$ is greater than that of $D_y^{3+}–TiO_2$.

**Keywords:** titanium dioxide; dysprosium doped; reduced graphene oxide; citric acid; photocatalysis

## 1　Introduction

Titanium dioxide ($TiO_2$) is the most popular photocatalyst for wastewater treatment and air remediation due to its non-toxicity, low cost, favorable optoelectronic property, excellent chemical stability and high reactivity [1–3]. However, the band gap of anatase $TiO_2$ is approximately 3.2 eV, which can only be activated by ultraviolet (UV) light (＜5% of sunlight) and thus seriously reduces its sunlight utilization. Moreover, the fast recombination of photogenerated electron–hole pairs decreases the photocatalytic quantum efficiency. Many efforts have been devoted toimproving the catalytic efficiency of $TiO_2$, such as doping with metal or nonmetal ions, depositing noble metal, coupling anatase $TiO_2$ with other narrow band gap semiconductors, *etc.*. Among them, ion doping is more effective in improving the photocatalytic activity of $TiO_2$ [4].

收稿日期：2015–10–23。　修订日期：2016–01–05。
基金项目：省部共建有色金属先进加工与再利用国家重点实验室开放课题(SKLAB02015010)和甘肃省自然科学基金(1112RJ2A013)资助。
第一作者：李翠霞(1972—)，女，博士，副教授。

**Received date:** 2015–10–23.　**Revised date:** 2016–01–05.
**First author:** LI Cuixia (1972–), female, Ph.D., Associate Professor.
**E-mail:** licx2007@lut.cn

As a new type of carbon nano–material, graphene has many outstanding potential applications in the field of lithium ion batteries, solar cells, heterogeneous catalysis, electronic information materials, *etc.* [5–6]. Its unique and outstanding properties include excellent electron conductivity, high thermal properties and large specific surface area. Recent researches showed that the $TiO_2$ and reduced graphene oxide (*r*GO) composite accelerated the interfacial electron transfer rate, effectively suppressed the recombination of photogenerated electrons and holes, improved the physical and chemical adsorption of organic matter, and enhanced the photocatalytic activity[7–9]. However, *r*GO is hydrophobic, while $TiO_2$ is hydrophilic. Therefore, solving this incompatibility and obtaining better photocatalytic activity of composite photocatalysts become a key issue.

If *r*GO/$TiO_2$ composite photocatalysts were doped with metal or nonmetal ions, the photocatalytic activity could be improved further [10]. In this paper, citric acid was used as a hydrolysis inhibitor of tetrabutyl titanate and a surfactant of graphene oxide (GO). GO/$D_y^{3+}$–$TiO_2$ was prepared by a one-step sol–gel method and subsequently reduced by sodium borohydride after annealing to obtain *r*GO/$D_y^{3+}$–$TiO_2$ composites. The effect of GO on the crystal structure of $TiO_2$ was investigated, including the lifetime of photogenerated carriers, and the morphology and photocatalytic activity of composite photocatalysts.

# 2 Experimental

## 2.1 Sample preparation

$D_y^{3+}$–$TiO_2$ composites were prepared *via* the sol–gel method. 3.5 g of citric acid (≥99.5%) was dissolved in 25 mL anhydrous ethanol (≥99.7%) under stirring at room temperature. Following this, 1 ml of 0.026 46 g/Ml dysprosium nitrate solution was added and stirred for 10 min, and then 5 mL tetrabutyl titanate (≥98%) was injected and stirred for 30 min (solution A). Then, 1 mL of distilled water was added dropwise to solution A under vigorous stirring. A $D_y^{3+}$–$TiO_2$ precursor sol was obtained after stirring for 2 h. Under the same conditions, we could obtain a $TiO_2$ precursor sol without the dysprosium nitrate solution. After the $D_y^{3+}$–$TiO_2$ sol was dried at 100 ℃ for 24 h, the $D_y^{3+}$–$TiO_2$ xerogel was ground and then calcinated in a muffle furnace at 450 ℃ for 3 h to obtain $D_y^{3+}$–$TiO_2$ composites (sample a).

GO was prepared following the Hummers method [11] using natural graphite (0.300 mm). GO was added to distilled water (in a beaker) and placed in a bath ultrasonicator for 1 h to yield a light-brown homogeneous GO suspension. Part of GO suspension was deoxygenated using a certain amount of sodium borohydride (≥98%). The color of the solution changed from light-brown to black under vigorous stirring for 30 min. The resultant graphene suspension was centrifuged and washed with plenty of distilled water and then collected and dried to obtain black *r*GO (sample f). The rest of the GO suspension was centrifuged and then dried into solid GO.

$D_y^{3+}$–$TiO_2$ precursor sol was mixed with GO at 5% (in mass fraction), 10%, 15%, 20% (samples b, c, d, e, respectively) under vigorous stirring, and then the mixture was ultrasonically agitated for 30 min to obtain the precursor sol of GO/$D_y^{3+}$–$TiO_2$. In the same way, we could obtain the precursor sol of GO/$TiO_2$ (sample g) by mixing 10% GO with the $TiO_2$ precursor sol. The precursor sol was processed by drying, grinding, and then calcinating at 450 ℃ for 3 h to form GO/$D_y^{3+}$–$TiO_2$ and GO/$TiO_2$ composites. Lastly, *r*GO/$D_y^{3+}$–$TiO_2$ and *r*GO/$TiO_2$ composites were prepared by sodium borohydride reduction.

## 2.2 Characterization

The crystalline structure and crystallite size of samples were investigated by a model D8 advanced X-ray diffractometer (XRD) using the copper (Cu) $K_{\alpha 1}$ line. The operating conditions were controlled at a voltage of 40 kV and a current of 40 mA. The scanning range varied from 20º to 70º with a scanning rate of 0.02 (º)·$s^{-1}$. The $TiO_2$ crystallite sizes were estimated from the full width at half maximum (FWHM) of XRD patterns using the Scherrer equation. The Raman spectrum of the sample from 1 100 $cm^{-1}$ to 3 000 $cm^{-1}$ was carried out by a micro-Raman spectroscope (JY-HR800, Horiba, Paris, France) with 532 nm laser excitation. A model Tecnai $G^2$F20 transimission electron microscope (TEM) was operated at 200 kV to observe the morphology of the composites. Fluorescence emission spectra were recorded from 350 to 500 nm on a model F97 Pro fluorospectro-photometer at ambient temperature. The excitation wavelength of the xenon lamp was 310 nm.

## 2.3 Photocatalytic activity

In a typical process, 0.10 g of photocatalyst was dispersed in 100 mL of 10 mg/L methyl orange solution (pH=3) in a bath ultrasonicator for 5 min. Prior to illumination, the suspension was magnetically stirred in the dark for 30 min to ensure the establishment of an adsorption-desorption equilibrium between the photocatalyst nanoparticles and methyl orange. Subsequently, 2 mL of hydrogen peroxide solution was dropped into the suspension; then, the suspension was irradiated with a 250 W high pressure mercury lamp. The distance between the light source and the surface of the reaction solution was 15 cm to keep the reaction solution at ambient temperature. The entire apparatus was carefully set to prevent the ambient light from disturbing the photoreaction, which was carried out for 40 min. During light irradiation, 10 mL of the solution was sampled every 10 min. The solution taken out was centrifuged at 8 000 rpm to separate the photocatalyst and the concentration of the supernatant fluid was measured by a model 7230G visible spectrophotometer.

The photocatalytic efficiency formula is as follows:

$$\eta=\frac{c_0-c_t}{c_0}\times100\% \quad (1)$$

where $c_0$ is the initial concentration of methyl orange, and $c_t$ is the concentration of methyl orange after illumination at $t$ min.

# 3 Results and discussion

## 3.1 Structure and morphology

3.1.1 XRD analysis Figure 1 shows the XRD diffraction patterns of $D_y^{3+}$–$TiO_2$ and $r$GO/$D_y^{3+}$–$TiO_2$ composite hybrids formed at various GO mass percentages. The characteristic peaks of $D_y^{3+}$–$TiO_2$ (sample a) at $2\theta$=25.3°, 37.8°, 48.2°, 54.0° and 62.8° are assigned to (101), (004), (200), (105), and (204) planes of anatase–$TiO_2$ (JCPDS No. 89-4921). The rest of the well-resolved peaks of sample at $2\theta$=27.5° and 36.2° can be indexed as (110) and (101) plane reflections of rutile-$TiO_2$ (JCPDS No. 89–4920). Clearly, the $D_y^{3+}$–$TiO_2$ processes produce mixed anatase and rutile phases. However, the XRD patterns of samples b, c, d, and e show that $r$GO/$D_y^{3+}$–$TiO_2$ composite hybrids formed at various GO mass fraction are a single anatase phase. This indicates that the addition of GO has an influence on the phase structure of the $TiO_2$, and inhibits the phase transformation from anatase to rutile. In addition, the average crystal sizes of the anatase nanoparticles were obtained from the Scherrer equation. The calculated mean crystallite size of sample a is 8 nm, and those of samples b, c, d and e are approximately 7 nm (according to the (101) plane characteristic peak calculation), as shown in Table 1. Because the two-dimensional plane structure of graphene as a carrier can improve the dispersion degree of $TiO_2$ in the $TiO_2$ and graphene composites [12–13], it is thus concluded that the addition of GO can effectively inhibit the grain size of $TiO_2$ gathering and growing up. As a result, a smaller grain size of $TiO_2$ can be obtained.

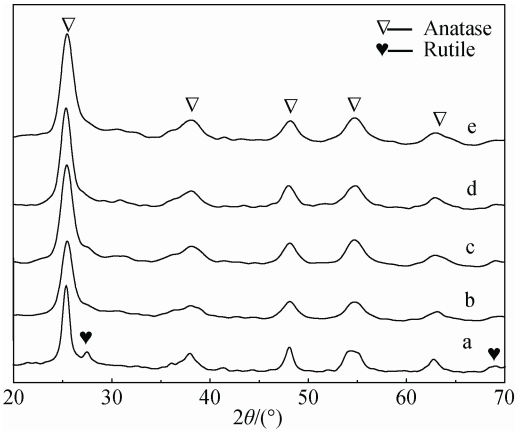


Fig. 1 XRD patterns of $D_y^{3+}$–$TiO_2$ (sample a) and $r$GO/$D_y^{3+}$–$TiO_2$ composites hybrids formed at various mass fraction of GO

**Table 1 Crystal size of $D_y^{3+}$–$TiO_2$ (sample a) and $r$GO/$D_y^{3+}$–$TiO_2$ composites hybrids formed at various mass fraction of GO**

| Sample | a | b | c | d | e | e |
|---|---|---|---|---|---|---|
| Crystal size/nm | 8.0 | 7.1 | 7.0 | 6.8 | 6.8 | 6.8 |

Notably, the characteristic diffraction peaks of graphene (002) at approximately 26° do not appear in the XRD pattern because a large number of $TiO_2$ attached to the surface of graphene and the characteristic diffraction peaks are covered [14]. No obvious diffraction peak of $D_y$–containing materials in XRD patterns of $r$GO/$D_y^{3+}$–$TiO_2$ may be due to their low content and high dispersion.

3.1.2 Raman analysis Figure 2 shows the Raman spectrum of sample c. In Fig. 2, the $D$ band (1 382 $cm^{-1}$), $G$ band (1 612 $cm^{-1}$) and $G'$ band (2 711 $cm^{-1}$) of $r$GO can be found. This further confirms that $r$GO appears in the composite. The $G$ band is a doubly degenerate (ITO and ILO) phonon mode ($E_{2g}$ symmetry) at the Brillouin zone center, whereas the $D$ band is due to phonon branches around the $K$ point and requires a defect for its activation. The $G'$ band is due to a double resonance intervalley Raman scattering process with two ITO phonons at the $K$ point [15]. Electron and hole doping cause the characteristic peak of $r$GO red shift [16] compared to the results of Wu *et al*. [17].

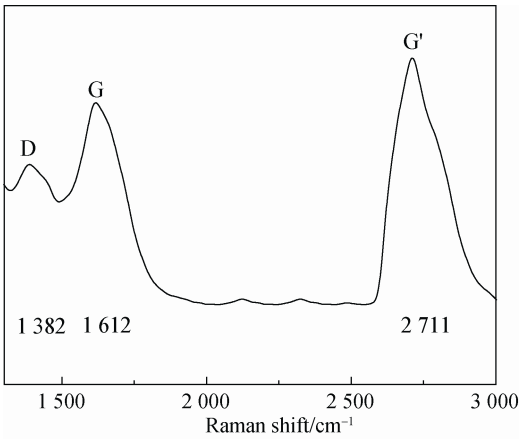


Fig. 2 Raman spectrum of sample c

3.1.3 TEM analysis Figure 3(a) shows the typical TEM image of composite photocatalysts (sample c). The randomly dispersed dark spots on the $r$GO background are due to the presence of $D_y^{3+}$–$TiO_2$ nanoparticles (The XRD pattern of $r$GO/$D_y^{3+}$–$TiO_2$ (see Fig. 1 (c)) confirm its existence). It is seen that the crystallites with uniform size have less agglomerate phenomena and are well distributed on the surface of $r$GO. $D_y^{3+}$–$TiO_2$ nanocrystals directly grown on graphene exhibits strong interactions with the underlying GO sheets because sonication does not lead to their dissociation from the sheets. This may be because citric acid causes the unidentate complexing

reaction with tetrabutyl titanate precursor or $D_y^{3+}$, as shown in formulas (2) or (3). The complexing reaction replaces parts of the precursor alkoxy and forms the compound with a larger space steric hindrance, which effectively reduces the hydrolysis rate of the precursor and prevents the formation of large particles in the sol–gel process. Therefore, a stable sol is obtained, resulting in the uniform doping of $D_y^{3+}$ [18–19].

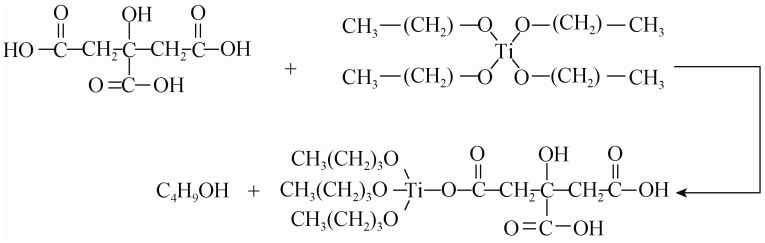

(2)

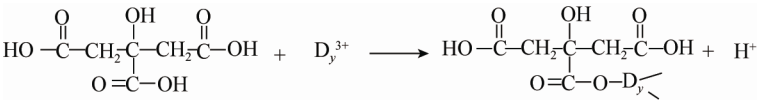

(3)

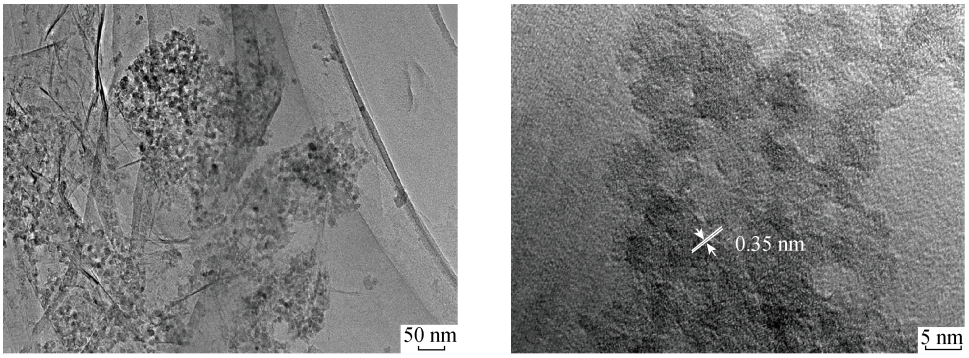


(a) TEM image　　(b) HRTEM image

Fig. 3　TEM and HRTEM images of sample c

GO contains massive hydroxyl and carboxyl, epoxy groups, *etc*., among them, hydroxyl and epoxy functional groups are mainly on the surface of graphene while carbonyl and carboxyl are at the edge of the graphene [20]. In addition, one citric acid molecule contains a hydroxyl and three carboxylic acid groups. In addition to the one forming the complexing group, the other hydroxyl and carboxyl groups of citric acid can react with most of the carboxyl and hydroxyl groups of GO, forming a complex compound with molecular shape evenly distributed on the surface of the GO. Then, *r*GO/$D_y^{3+}$–$TiO_2$ composites are synthesized in situ *via* heat treatment and sodium borohydride reduction. Figure 4 shows the possible reaction mechanism.

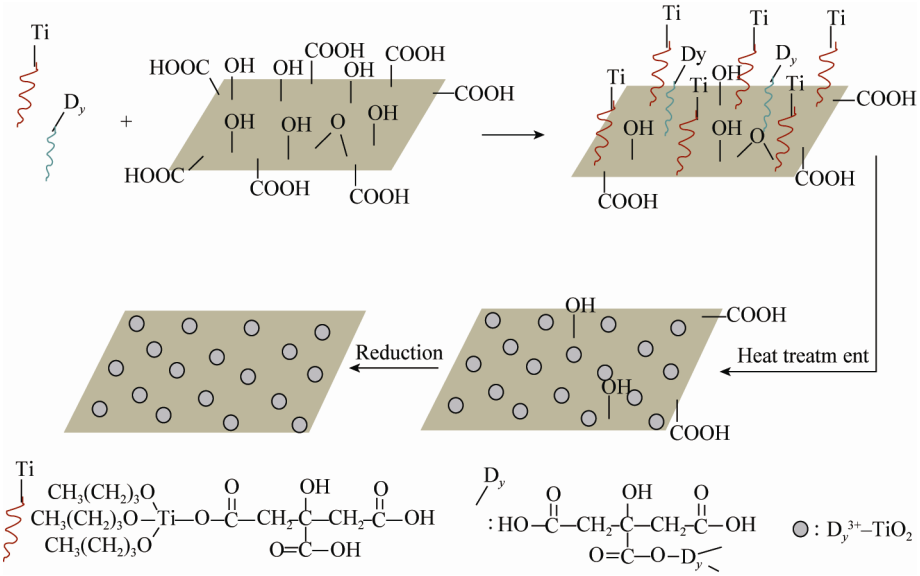


Fig. 4　Schematic presentation of *r*GO/$D_y^{3+}$–$TiO_2$ preparation

The HRTEM image of *r*GO/$D_y^{3+}$–$TiO_2$ composite (see Fig. 3 (b)) shows that most of the $D_y^{3+}$–$TiO_2$ nanoparticles are approximately 6–8 nm in size, and the interplanar spacings of the adjacent lattice fringe are estimated to be approximately 0.35 nm, corresponding to the (101) plane of the anatase–$TiO_2$ lattice [21], consistent with the XRD pattern (see Fig. 1(c)).

3.1.4 Photoluminescence (PL) spectra analysis

Semiconductor photocatalysts excited by light can produce photogenerated electrons and holes, part of which can recombine and fluoresce in the meantime. The higher intensity of fluorescence indicates a higher recombination rate of photogenerated electrons and holes. On the contrary, a lower intensity of fluorescence represents the more effective separation of photogenerated electron–hole pairs [22–23]. The PL spectra of the samples (see Fig. 5) show that the fluorescence emission spectrum relative intensity for all the samples is in the sequence of a > e > d > b > c. This indicates that the introduction of *r*GO can reduce the recombination rate and extend the carrier life of photogenerated electrons and holes to improve the photocatalytic efficiency of composites. With the increment of GO, the recombination rate of photogenerated electrons and holes increases again after a decline. The recombination rate of sample c with 10% GO introduction is the samllest and the photogenerated carrier life is the longest, indicating the greatest photocatalytic efficiency at a 10% introduction amount. The long life of carriers can be a result of the strong coupling between $TiO_2$ and *r*GO, which facilitates interfacial charge transfer (with *r*GO as an electron acceptor) and inhibits electron–hole recombination [24]. However, *r*GO is also a type of recombination center, and too much *r*GO can promote the recombination of photogenerated electrons and holes [25]. In addition, the addition of excess GO leads to the aggregation of GO; correspondingly, the amount of the active components ($D_y^{3+}$–$TiO_2$) that generate carriers on the GO sheet is reduced.

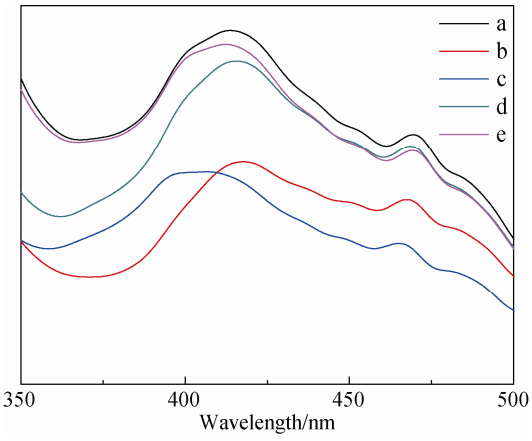


Fig. 5 Photoluminescence spectra of different samples

### 3.2 Photocatalytic activity

The photocatalytic activity of *r*GO/$D_y^{3+}$–$TiO_2$ formed at various GO mass percentages was evaluated using methyl orange under UV irradiation and compared with that of $D_y^{3+}$–$TiO_2$ nanocrystals synthesized *via* the same method in the absence of GO and *r*GO. Figure 6 shows the results. Clearly, methyl orange is slightly degraded in the presence of *r*GO (sample f), but *r*GO/$D_y^{3+}$–$TiO_2$ photocatalyst exhibits better photocatalytic activity than that of $D_y^{3+}$–$TiO_2$. When the amount of GO is 10%, the degradation rate of methyl orange is 92.95%.

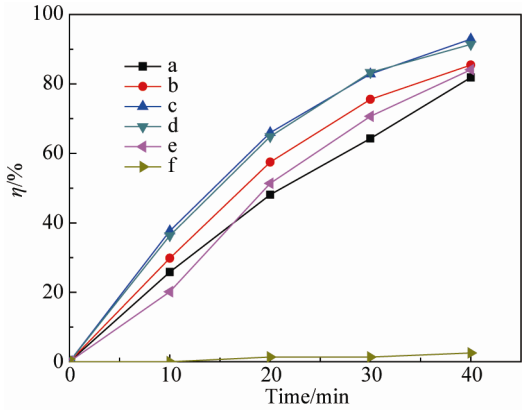


Fig. 6 Photocatalytic activity of different samples

The results can be attributed to two factors. First, the excellent electron conductivity of *r*GO is beneficial to separate electron–hole pairs. Accordingly, it can improve the photocatalytic activity of the composites. Second, the lamellar structure of *r*GO has a great specific surface area and the conjugated structure can adsorb many pollutants and provide desired reacting sites for photocatalytic reaction [26]. However, as excess *r*GO is added, their effect on degradation becomes worse because excess *r*GO can act as recombination centers of photogenerated electron–hole pairs. At the same time, effective components of $D_y^{3+}$–$TiO_2$ are also reduced due to the aggregation of *r*GO, thus reducing the photocatalytic activity of *r*GO/$D_y^{3+}$–$TiO_2$ composites.

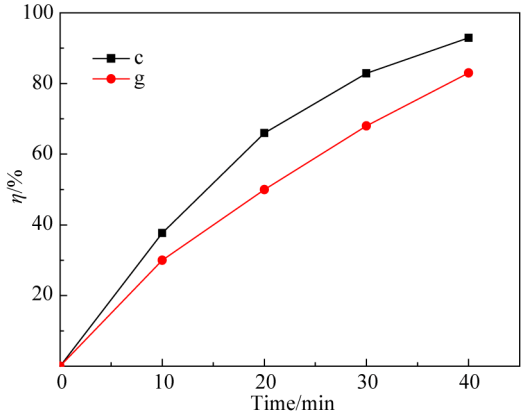


Fig. 7 Photocatalytic activity of *r*GO/$D_y^{3+}$–$TiO_2$ (sample c) and *r*GO/$TiO_2$ (sample g)

Figure 7 shows the photocatalytic activity of *r*GO/$D_y^{3+}$–$TiO_2$ (sample c) and its reference sample *r*GO/$TiO_2$ (sample g). Clearly, *r*GO/$D_y^{3+}$–$TiO_2$ photocatalyst exhibits better photocatalytic activity than that of *r*GO/$TiO_2$. This is because $D_y^{3+}$ doping inhibits the growth of anatase $TiO_2$ crystallite (The calculated mean crystallite size of sample g is 11.0 nm). Meanwhile, the presence of rare-earth in the $TiO_2$ crystal lattice can decrease the band gap and accelerate the separation of photogenerated electron–hole pairs, eventually leading to a greater photocatalytic activity [27–28].

# 4 Conclusions

*r*GO/$D_y^{3+}$–$TiO_2$ composite materials were in situ synthesized *via* citric acid chelating sol–gel step, followed by annealing and reducing. The photocatalytic activity of the *r*GO/$D_y^{3+}$–$TiO_2$ composites was obviously better than $D_y^{3+}$–$TiO_2$ and associated with the additional amount of GO in the preparation process. Citric acid acted as a hydrolysis inhibitor of tetrabutyl titanate and a surfactant of GO. This method produced a hybrid structure with strong interactions between *r*GO and $D_y^{3+}$–$TiO_2$. The strong coupling could form advanced hybrid materials for various applications, including photocatalysis, $TiO_2$-based electrodes for lithium ion batteries, supercapacitors and dye-sensitized solar cells, in which strong electrical coupling to $TiO_2$ nanoparticles was also important.

**References:**


[1] SHEN X, ZHU L, LIU G, et al. Enhanced photocatalytic degradation and selective removal of nitrophenols by using surface molecular imprinted titania[J]. Environ Sci Technol, 2008, 42(5): 1687–1692.

[2] WANG N, ZHU L, HUANG Y, et al. Drastically enhanced visible-light photocatalytic degradation of colorless aromatic pollutants over $TiO_2$ *via* a charge-transfer-complex path: a correlation between chemical structure and degradation rate of the pollutants[J]. J Catal, 2009, 266(2): 199–206.

[3] AN G M, MA W H, SUN Z Y, et al. Preparation of titania/carbon nanotube composites using supercritical ethanol and their photocatalytic activity for phenoldegradation under visible light irradiation[J]. Carbon, 2007, 45(9): 1795–1801.

[4] LOZOVSKYI O, GÜNDÜZ G, DÜKKANCI M, et al. Preparation and characterisation of silver– or copper-doped $TiO_2$ catalysts and their catalytic activity in dye degradation[J]. Color Technol, 2015, 131(3): 245–254.

[5] TANG L, WANG Y, LI Y, et al. Preparation, structure, and electrochemical properties of reduced graphene sheet films[J]. Adv Funct Mater, 2009, 19(17): 2782–2789.

[6] XU P T, YANG J X, WANG K S, et al. Porous graphene: Properties, preparation, and potential applications[J]. Chin Sci Bull, 2012, 57(23): 2948–2955.

[7] LIGHTCAPI V, KOSEL T H, KAMAT P V. Anchoring semiconductor and metal nanoparticles on a two-dimensional catalyst Mat. storing and shuttling electrons with reduced graphene oxide[J]. Nano Lett, 2010, 10(2): 577−583.

[8] XIANG Q J, YU J G, JARONIEC M. Graphene–based semiconductor photocatalysts[J]. Chem Soc Rev, 2012, 41: 782−796.

[9] ZHAO H M, SU F, FAN X F, et al. Graphene–$TiO_2$ composite photocatalyst with enhanced photocatalytic performance[J]. Chin J Catal, 2012, 33(5): 777−782.

[10] ZHANG X Y, SONG Z J, ZHOU F Z, et al. Synthesis of F, N Co–doped $TiO_2$ decorated reduced graphene oxide and its visible light photocatalytic properties[J]. J Chin Ceram Soc, 2015, 43(7): 919–925.

[11] HUMMERS W S, OFFEMAN R E. Preparation of graphitic oxide[J]. J Am Chem Soc, 1958, 80(6): 1339–1339

[12] CHEN J S, XU Q H. Synthesis and thermal properties of citric acid titanium (IV) compounds[J]. J Yunnan Univ: Nat Sci Ed, 1999, 21(4): 309–311.

[13] EDA G, FANCHINI G, CHHOWALLA M. Large–area ultrathin films of reduced graphene oxide as a transparent and flexible electronic material[J]. Nature Nanotech, 2008, 3(5): 270–274.

[14] SHEN L, ZENG M, YANG S W, et al. Electron transport properties of atomic carbon nanowires between graphene electrodes[J]. J Am Chem Soc, 2010, 132(33): 11481–11486.

[15] VOGGU R, DAS B, ROUT C S, et al. Effects of charge transfer interaction of graphene with electron donor and acceptor molecules examined using Raman spectroscopy and cognate techniques[J]. J Phys Condens Mat, 2008, 20(47): 1005–1008.

[16] TUINSTRA F, KOENIG J L. Raman Spectrum of graphite[J]. J Chem Phy, 1970, 53(3): 1126–1130.

[17] WU J X, XU H, ZHANG J. Raman spectroscopy of graphene[J]. Acta Chim Sin, 2014, 72(3): 301–318.

[18] SHA M J. Photoluminescence properties of $(Er,Y)_2Ti_2O_7$ nanocrystalline powders prepared by a citric acid chelated sol–gel method[D]. Dalian: Dalian Univ Tech, 2007.

[19] GENG J Y, ZHU X S, DU Y K. $TiO_2$–graphene photocatalyst:preparation and effect of the introducation of graphene on photocatalytic performance[J]. Chin J Inorg Chem, 2012, 28(2): 357–361.

[20] KOVTYUKHOVA N I, OLLIVIER P J, MARTIN B R, et al. Layer-by-layer assembly of ultrathin composite films from micron–sized graphite oxide sheets and polycations[J]. Chem Mater, 1999, 11(3): 771–778.

[21] LI F B, LI X Z. Photocatalytic properties of gold/gold ion–modified titanium dioxide for wastewater treatment[J]. Appl Catal A: Gen, 2002, 228(1): 15–27.

[22] ZHANG J, MINAGAWA M, AYUSAWA T, et al. In situ investigation of the photocatalytic decomposition of NO on the Ti-HMS under flow and closed reaction systems[J]. Phy Chem B, 2000, 104(48): 11501–11505.

[23] WANG D T, LI X, CHEN J F, et al. Enhanced photoelectrocatalytic activity of reduced graphene oxide/$TiO_2$ composite films for dye degradation[J]. Chem Eng J, 2012, 198–199: 547–554.

[24] WANG, W D, SERP P, KALCK P, et al. Photocatalytic degradation of phenol on MWNT and titania composite catalysts prepared by a modified sol–gel method[J]. Appl Catal B, 2005, 56, 305–312.

[25] ZHOU X W, ZHU Z L, ZHAO J K et al. Research on $TiO_2$/CdS coupled semiconductor photocatalytic degradation of methyl orange in wastewater[J]. Tech and Equip Environ Pollut Control, 2006, 7(1): 106–109.

[26] CEN J W, LI X J, HE M J, et al. Effects of $La^{3+}$ non–uniformly doping in $TiO_2$ films on photocatalytic activities [J]. J Mater Sci Technol, 2005, 23(6): 668–673.

[27] SUN D F, WANG K, XU Z J, LI R X. Synthesis and photocatalytic activity of sulfate modified $N_d$-doped $TiO_2$ under visible light irradiation[J]. J Rare Earth, 2015, 33(5): 491–497.

[28] HASSAN M S, AMNA T, YANG O B, et al. $TiO_2$ nanofibers doped with rare earth elements and their photocatalytic activity[J]. Ceram Int, 2012, 38(7): 5925–5930.